# Characteristics of a new dust coordinate sensor



2012 Meas. Sci. Technol. 23 105902

(http://iopscience.iop.org/0957-0233/23/10/105902)

Meas. Sci. Technol. **23** (2012) 105902 (6pp) doi:10.1088/0957-0233/23/10/105902

# Characteristics of a new dust coordinate sensor

**Paige Northway[1,2], Siegfried Auer[3], Keith Drake[1,2], Mihaly Horanyi[1,2], Anna Mocker[1,2,4], Tobin Munsat[1,2], Anthony Shu[1,2], Zoltán Sternovsky[1,2], Evan Thomas[1,2] and Jianfeng Xie[1,2]**

[1] Laboratory for Atmospheric and Space Physics, University of Colorado, 1234 Innovation Drive, Boulder, CO 80303, USA
[2] Colorado Center for Lunar Dust and Atmospheric Studies, University of Colorado, Boulder, CO 80303, USA
[3] A&M Associates, PO Box 421, Basye, VA 22810, USA
[4] Institut für Raumfahrtsysteme, Universität Stuttgart, Pfaffenwaldring 31, D-70569 Stuttgart, Germany

E-mail: paige.northway@colorado.edu

Received 29 March 2012, in final form 13 July 2012
Published 11 September 2012
Online at stacks.iop.org/MST/23/105902

**Abstract**
A new in-beam dust coordinate sensor (DCS) at the Colorado Center for Lunar Dust and Atmospheric Studies (CCLDAS) dust accelerator facility has been constructed and is now in use. The dust sensor operates by measuring the image charges induced on two planes of wire electrodes by passing charged dust particles. Applications for the DCS include the quantitative evaluation and improvements of the focusing and steering elements of the accelerator, and the correlation of particle velocity and mass with impact sites using precision particle location. For focusing and steering improvements, particle positions to 0.25 mm are plotted in real-time. It is possible to determine a typical particle's position within the beamline to $< 0.1$ mm. The design, simulation and results of the DCS are further discussed.

**Keywords:** beam monitor, charge induction, coordinate sensor, dust accelerator

(Some figures may appear in colour only in the online journal)

## 1. Introduction

Dust detection instruments have been used in space for the investigations of the properties of cosmic dust in the solar system over the last 50 years [1–4]. These instruments detect the particles impinging onto a target via the physical processes which originate from these events. Examples of this include the emergence of an impact ionization plasma from a metal plane target [5] and the track of a particle collected in aerogel [6].

To calibrate instruments for *in situ* measurements, hypervelocity impact measurements under similar, well-defined conditions are required. To this end, micrometer and sub-micrometer sized particles are charged in a dust source [8], passed into a homogeneous accelerating field and focused onto the investigating instrument. An accelerator of this type is installed at the University of Colorado, Boulder, which utilizes a 3 MV Pelletron electrostatic accelerator[5]. A schematic of the accelerator, run by the Colorado Center for Lunar Dust and Atmospheric Studies (CCLDAS), is depicted in figure 1. A full description of the CCLDAS accelerator can be found in Shu *et al* [7], and a similar facility at the Max Planck Institut für Kernphysik is described in Mocker *et al* [9].

The characteristics of accelerated particles range from velocities of less than 1 km $s^{-1}$ to tens of km $s^{-1}$ and radii of 50 nm to 1.5 $\mu$m, approximately. The beamline particle selection unit includes velocity and mass detection and particle down-selection based on those properties.

A dust coordinate sensor (DCS) has been developed which uses the ratios of charge induced on wire electrodes by passing charged particles to determine the individual particle positions. Collectively, these individual particles make up

[5] National Electrostatics Corp., 7540 Graber Road, PO Box 620310, Middleton, WI 53562-0310, USA.

 

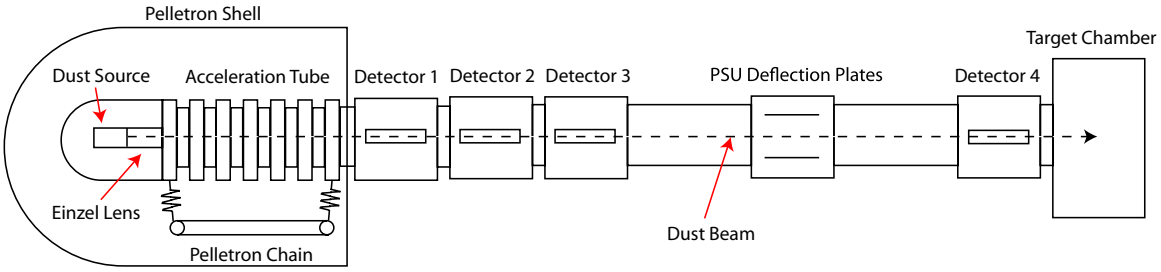


**Figure 1.** Schematic of the CCLDAS dust accelerator. The dust beam originates from the dust source, where particles become positively charged. The electrostatic field then accelerates the charged particles. The particles are detected and characterized while passing through the beamline detectors and down-selected based on their velocity by a particle selection unit (PSU). (From Shu *et al* [7].)

the beam profile. The detector outputs immediate feedback on the quality of the focusing and steering of the beam to maximize the number of particles reaching the target. Additionally, it provides the possibility of coordinating exact particle characteristics (mass, velocity) with individual impact sites. The information from the position detector could also be combined with particle selection information from the velocity detectors. This would allow the control parameters of the Einzel lens focusing (in figure 1) to be optimized for particular velocity ranges [9].

The basic instrument concept and design are presented in section 2. Electrostatic calculations critical to the interpretation of the detector signals are presented in section 3. Finally, the methods of interpreting instrument signals and calculations for the precision of the measurement are presented in section 4.

## 2. Measurement method and mechanical design

### *2.1. Charge detection by induction*

The DCS uses the principle of induction to determine a dust particle's location in the beamline. As a charged dust particle approaches a conducting electrode (in this case a wire), image charges flow to the electrode from ground, and are recorded by high-gain charge sensitive amplifiers (CSAs) [10]. The measured induced charge can then be compared to the expected response, enabling the determination of the charge of the dust particle. While the image charges are linearly related to particle charge through a response coefficient, the determination of this coefficient can be complicated. In general, the analytical calculation of the response coefficient of the wires is complex, due to the complicated geometry of the detectors (including multiple wires and ground planes). Simplified analytical calculations for charge induced on an infinite wire within a plane of wires are described by Xie *et al* [11]. For more complicated geometries, finite-element simulations have been performed using the COULOMB software package.

### *2.2. Dust coordinate sensor design*

The DCS was developed for the CCLDAS dust accelerator facility and utilizes the measurement of charge induced by particles penetrating two orthogonal planes of four wires to pinpoint the *xy*-position of each particle. The design of the DCS borrows a number of design elements

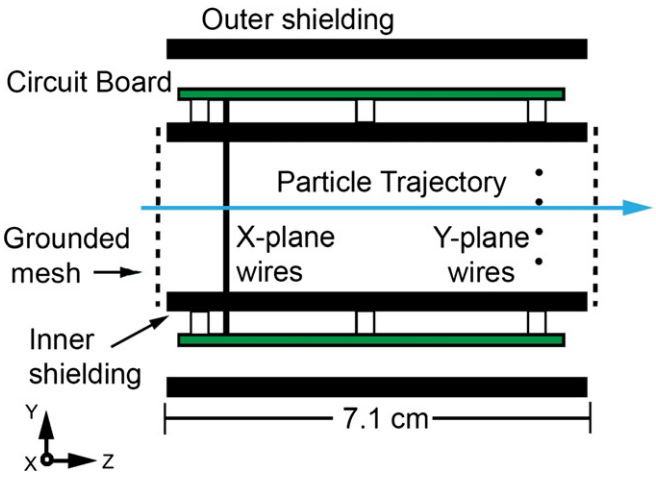


**Figure 2.** Schematic cross-section of the wire-grid detector. Inner and outer shielding, circuit boards, grounded mesh and both planes of wire electrodes are shown. Distances are to scale, a notable dimension being the 5.1 cm between wire planes.

from the dust trajectory sensor (DTS) [11–13], including shielding/grounding concepts and detection circuitry.

The physical design of the detector is driven by the size constraints of fitting the detector body, electronics and electrostatic shielding into the vacuum hardware of the beamline. For versatile compatibility, the detector is mounted onto a DB-25 feedthrough flange by a 10 cm extension arm and can be placed in a 15.2 cm (6″) CF cross or tee. This requires that the detector and mounting arm fit through a cylinder with radius 5 cm and not extend from the center of the beamline past an arc of the same radius. The shielding requirements include separate grounded Faraday cage shielding for the wire electrodes and the electronics to limit noise in the signals. Two final considerations are the need to be as transparent to dust particles as possible (since the detector remains in the center of the beamline during experiments) and a signal output system that allows for real-time plotting of particle positions.

Within these limitations, the detector design shown in figure 2 was developed. The inner and outer shielding are made from 3.2 mm thick aluminum square channel with inner dimensions of 2.5 and 5.7 cm, respectively. They are 7.1 cm long, with the wire electrode planes recessed 1 cm from either end of the inner shielding, leaving 5.1 cm between the two planes. In addition to the inner and outer shielding, the open ends of the detector are shielded by a grounded

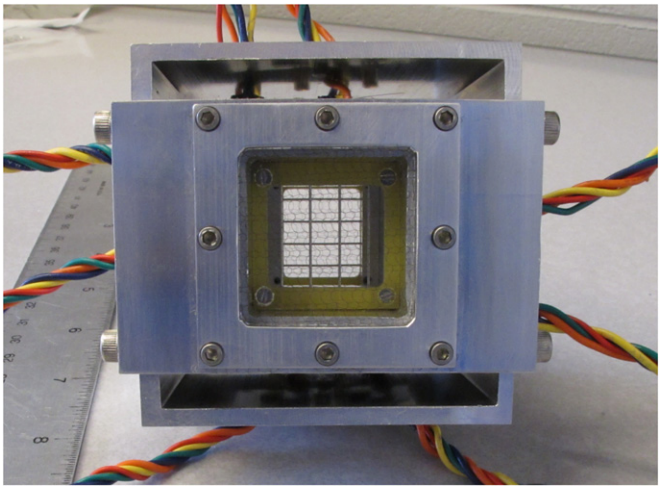

**Figure 3.** Front view of the assembled detector. The eight screws visible on the front of the detector secure the grounded mesh between the two plates at the entrance. The 0.48 mm thick wire electrodes in the *x*- and *y*-directions are visible in the middle.

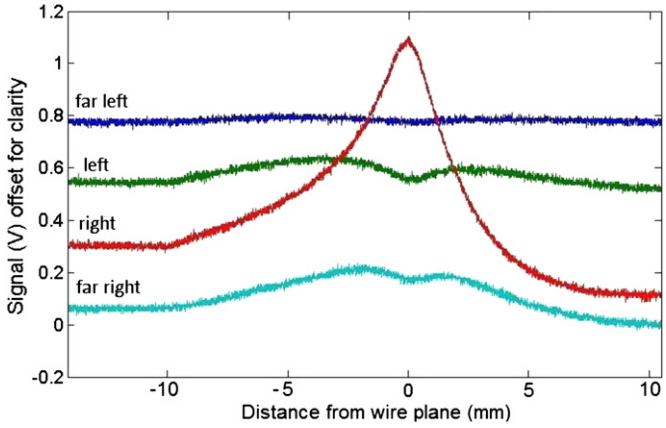


**Figure 4.** Signals from the *x*-plane of the wire-grid detector where a particle with a charge of approximately 80 fC passes just to the left of the inner right wire electrode, or approximately 3.4 mm right of center.

knitted wire mesh with an open area greater than 90%. The shielding mesh and wire electrodes are best displayed in the perspective of figure 3. The wire electrodes in the first plane run in the horizontal ($x$) direction and measure the vertical ($y$) position of the particles, while the wires in the second plane are orthogonal. There are four wires spaced 5 mm apart in each plane, dividing the planes of wires into five regions each, for a total of 25 regions within the center 6.25 $cm^{-2}$ of the beamline. The central nine of these regions are useful for precision positioning. Each of the components, i.e. inner shielding, outer shielding, and each of the eight circuits are connected to earth ground at only a single point. This minimizes signal distortion from grounding loops. The CSA circuits are printed with two electrically separate circuits per board and are mounted on the outside of all four sides of the inner shielding. The circuits are powered by battery supplies regulated to output $\pm 6$ V and $\pm 3.5$ V.

The key component to acquiring signals from passing dust particles is the high speed CSA circuit setup. Similar to the DTS circuitry setup described by Duncan [10], the wire electrodes of the DCS exit the inner shielding through small holes and connect directly to the CSA boards, which are mounted 3.8 mm outside of the inner shielding. This very small distance helps minimize electronic pickup noise in the signals. The electrodes are clamped between scored PCB board material, which effectively guides the wires through the small holes of the inner shielding to the boards. The sensor wires have a diameter of 0.48 mm, providing sufficient stiffness to remain straight. Each wire connects to a separate circuit with CSA sensitivity calibrated values ranging from 1.15 to $1.28 \times 10^{-13}$ V $C^{-1}$. The power supplies are monitored for any drop in voltage that could affect the calibrated sensitivities of the CSAs. The outputs of the circuits are sent through a DB-25 vacuum feedthrough to the data acquisition, where the rms noise on the signals is approximately 2 mV.

A sample of the signals recorded from the *x*-plane of wires created by a particle passing 3.4 mm to the right of center is displayed in figure 4. The CSA circuits are not capable of producing accurate signals for particles with velocities over the entire range of 1 to 100 km $s^{-1}$ because of the circuits' limited bandwidth (approximately 1 kHz to 10 MHz). The distortion of the signal is readily apparent on the right wire of figure 4 where the signal droops below zero after the peak. However, the distortion in the signal is corrected in the frequency spectrum by dividing by the transfer function of the electronics [10].

## 3. Simulation

The DCS was simulated using the COULOMB software package. The simulation contained the geometries of the wire electrodes, the inner shielding square tube and the grounded mesh at the openings of the shielding. The simulations included the calculation of charge induced on each wire from a particle in the plane of the wires over a grid of positions, in order to determine the ratios used for position detection. Charges induced on the wires as a function of the particle's distance from the plane of wires at a set *xy*-position were also simulated.

Figure 5 shows the percentage of particle charge induced on each wire in the plane measuring the *x*-position of the particle as the particle traverses the plane at a position 1.8 mm right of center and no vertical displacement from center. The dip at the center of the left and far right wires occurs as the proximity of the right wire acts as a sink of the induced particle charge. Simulations for particle trajectories through grids of wires with different geometries have also been conducted previously [14, 11]. The distortion in the signal apparent after the particle has passed the plane of the wires seen in the experimental data of figure 4 is an artifact of the circuit behavior, so it does not appear in the simulation.

The percentage of particle charge induced, not solely the ratios between wires, is taken into account when calculating the precision of the detector described in section 4.2, but it is of note that an average of 24%, with a standard deviation of 12% depending on position, of a particle's charge is lost to the walls of the inner shielding instead of being induced on the wires.

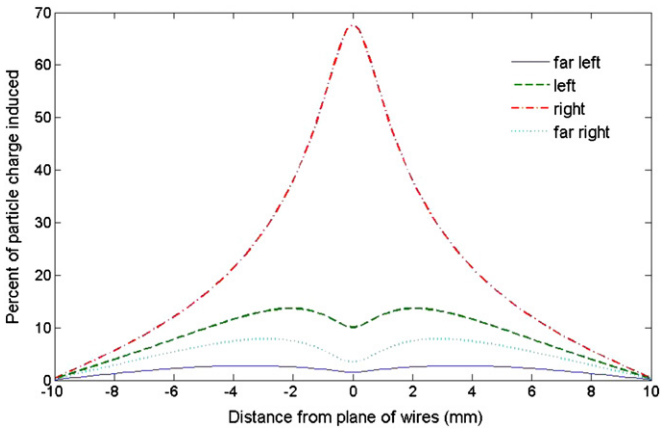


**Figure 5.** Simulated signals of the $x$-plane of wires where a particle is simulated traveling from 10 mm before the plane to 10 mm past the plane and the percentage of particle charge induced on each wire in the plane is plotted.

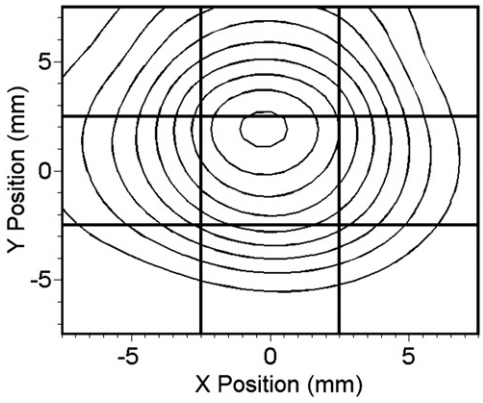


**Figure 6.** Beam profile contour generated with data from an unfocused, off-centered beam. In the plot, the center of the beam with the highest concentration of particles is located at $x = -0.25$ mm and $y = 2$ mm. Wire electrode locations are shown for reference, thickness not to scale.

## 4. Results

### *4.1. Interpretation of instrument signals*

There are two applicable approaches to data analysis. The first involves detailed analysis of the time-dependent waveforms generated by the detectors and results in the most accurate values for the position of individual particles [10, 11]. The second is a real-time analysis of the average beam size and placement over many particles. This method is primarily useful for finding optimal parameters for electrostatic focusing and steering of the beam.

For the most accurate determination of individual particle positions, the full waveforms of the output signals are considered. A fit is made of each waveform to minimize the effect of noise on the signals. The values of the fits from the two strongest signals (corresponding to the two closest electrodes) in each plane at the time of the highest peak are used to form the ratios. The ratios between the values of the two closest electrodes in each plane are then compared to simulated values to determine the $xy$-position of the particle.

Fitting the waveforms is computationally intensive and time consuming. Instead of using this method, the DCS is set up for the real-time mode of operation, which is carried out by a LABVIEW program. The program compares the charge induced on each of the eight wire electrodes with simulated charge induction for each of the eight wires. The simulated values for the eight electrodes are given for a grid of positions every 0.5 mm in the $x$- and $y$-directions over the area of the detector, and a bilinear interpolation is used to estimate the values on a grid of positions every 0.25 mm. The program then determines each particle at the position with the highest correlation of relative peak heights, within the computational grid. A contour plot of a surface fit of data from the wire-grid detector is shown in figure 6.

The possible particle velocities span two orders of magnitude. At the high-speed end, a particle traveling 50 km $s^{-1}$ produces a response from the detector in the form of a pulse of approximately 0.36 $\mu$s, which would require a data sample rate of 278 MHz to guarantee 100 samples over the duration of the pulse. For a particle with a velocity of 1 km $s^{-1}$, the same sample rate requires 5000 samples to span the pulse. To avoid the need for many samples at high sample rates across eight separate outputs, the signals are first passed through peak detector circuits. The circuits hold the peak value of a pulse with a decay rate of 250 mV $s^{-1}$ until reset, allowing for a much lower sample rate and eliminating the need for many samples.

A shortcoming of the peak detection method is the loss of the original waveforms from the detector. With the original waveforms, it is trivial to discern between waveforms corresponding to a passing particle and signals due to external noise sources. Using peak detection, the only information available is the height of the maximum voltage on each electrode, making false triggers non-obvious. To mitigate this problem, events in which the measured peak values do not match simulated values to 70% in each plane are discarded. Also, when determining the size of the beam and the position of the beam within the beamline using many particles, one false particle constitutes no observable effect. It is important to note that the peak detectors do not show the dip in the signal seen in figure 5, so the simulated values at the peak of these signals, approximately 2 mm from the plane of wires, were integrated in the calculations.

### *4.2. Instrument precision*

The precision of the DCS is determined using the simulated values for the fraction of a particle's charge induced on each wire and the equation

$$\sigma = \Delta r \cdot \left(\frac{\mathrm{d}p}{\mathrm{d}r}\right), \tag{1}$$

where $\sigma$ is the position uncertainty, $\Delta r$ is the error in the ratio and $\mathrm{d}p/\mathrm{d}r$ is the change in position for a change in ratio. The ratio, $r$, is defined as the charge induced by a particle carrying total charge of $Q$ on the wire electrode closest to the particle ($Q_1$) over that of the second closest wire ($Q_2$). The voltage of the output signal and the charge picked up by the CSA are interchangeable using the sensitivity of the circuit as the

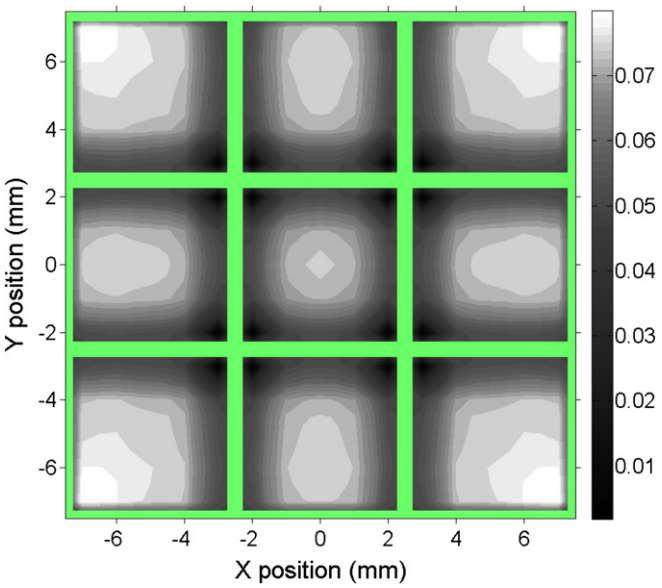


**Figure 7.** Detector uncertainty in position (mm) as a function of position within the detector for a sample particle with a charge of 16 fC under typical noise conditions. The wires are plotted as solid lines 0.48 mm wide. The uncertainty is low near the wires, as the change in the ratio of the induced charge is larger for a given change in position.

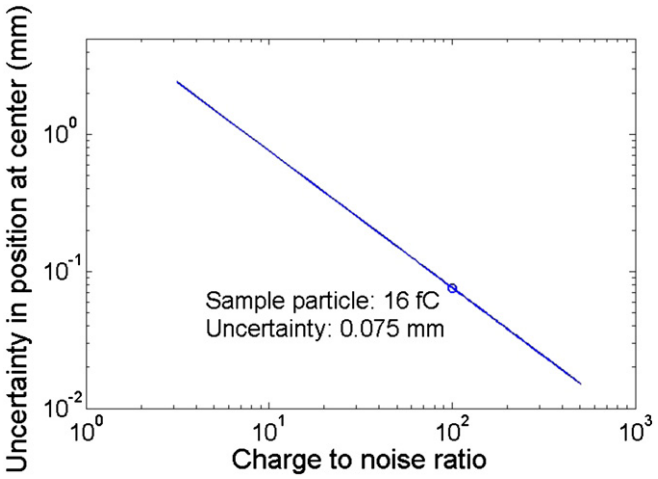


**Figure 8.** Uncertainty in position at the center of the detector as a function of QNRs.

conversion. $dp/dr$ is found by taking the inverse of the gradient of $r$ over a grid of positions. The ratios for this matrix originate from the COULOMB simulation results. The error in the ratio ($\Delta r$) is determined by

$$\Delta r = r \cdot \sqrt{\left(\frac{\Delta Q_1}{Q_1}\right)^2 + \left(\frac{\Delta Q_2}{Q_2}\right)^2}, \qquad (2a)$$

where $\Delta Q_{1,2}$ is the effective charge noise on the measured signal. The effective charge noise can, in fact, have contributions from many sources, such as gain error of the amplifiers, error of digitization and thermal noise. Given $\Delta Q = \Delta Q_1 = \Delta Q_2$ and defining the charge-to-noise ratio (QNR) equal to $Q/\Delta Q$, the QNR can be separated from the square root:

$$\Delta r = \frac{r}{\mathrm{QNR}} \cdot \sqrt{\left(\frac{1}{C_1}\right)^2 + \left(\frac{1}{C_2}\right)^2}, \qquad (2b)$$

where the fraction of a particle's charge induced on the nearest two wires is $C_{1,2}$.

The calculations for equation (1) are performed for both planes independently and added in quadrature to obtain a total uncertainty in position for a particle of given charge at any point within the detector. The results for a particle with a typical charge of 16 fC are depicted in figure 7. The charge of a typical particle was determined by the average charge recorded by the beamline detectors using a standard dust source. Near the wires (positioned at ±2.5 mm and ±7.5 mm in both directions), the error in the ratio is relatively large, but a large change in the ratio leads to only a small change in position, so the uncertainty is lowest. The opposite is true of the central region between two wires. At positions closer to the walls of the detector, the uncertainty increases because smaller signals are seen from the wires as more of the particle charge is induced on the wall. The wires themselves constitute a singularity. They are depicted as solid lines with the width of the wire, 0.48 mm, for graphical purposes. In practice, a particle that hits a wire ceases to be a usable particle, and the data are discarded.

Figure 8 displays how the uncertainty at the center of the detector scales with the QNR. Because the QNR can be kept separate until the final uncertainty calculation (2*b*), the entirety of the contour plot of figure 7 scales similarly. Assuming a constant noise from the circuits, an rms voltage of 2 mV, the uncertainty in position scales inversely with the charge on the particle. The sample particle, with charge 16 fC (QNR = 100) and an uncertainty in position of 0.075 mm, is shown for reference. For a 16 fC particle within the center square of the detector, the precision is 0.075 mm. If the beam of particles is not focused through the center square of the detector, the precision for 16 fC particle would be reduced to 0.083 mm. In the case of an unfocused beam, the wire-grid blocks 14% of the detector area, reducing the number of particles reaching the target. At the limit of being able to detect the position of a particle to within ±1 mm of its actual position anywhere within the detector, a minimum particle charge of $Q$ = 1.4 fC (QNR = 8.3) is required.

## 5. Summary

A dust coordinate sensor based on the principle of charge induction and comprising two orthogonal planes of four parallel wires each was designed and analyzed via experiments and simulations. The typical characteristics of particles detected with this new sensor are (positive) charge values down to 1 fC and velocities up to 100 km $s^{-1}$. The lower bound on the detectable charge is dictated by amplifier noise, which results in unacceptably high uncertainty in detected position when the charge-to-noise ratio is too low. The effective upper bound on both charge and velocity is dictated by the specifics of the data acquisition technique used. For charge, this means avoiding saturation of the final data acquisition stage; for detection of higher charge levels, the amplifier gains can simply be reduced.

For velocity, this means acquiring data at a sufficiently high rate to accurately capture the transient peak signals, which are critical for the position measurement. The accurate capture of the peaks can be improved with a combination analogue/digital circuit, as discussed in section 4.1.

To aid in the optimization of beam steering and focusing, the detector is used to provide an input to a plotting routine which records particle positions on a 0.25 mm grid in real-time, which sums to give the beam profile. To use the new detector for directly correlating individual particle characteristics to specific impact sites, the position measurements must be extremely precise. To address this requirement, the detector precision (as a function of the position and charge-to-noise ratio) was calculated based on simulations of the charge induced on each wire electrode. For a typical particle charge of 16 fC, the precision is 0.0825 mm anywhere within the detector. The position can be determined to a precision of $\pm 1$ mm for a particle carrying a charge as low as 1.4 fC.

## References


[1] Srama R *et al* 2004 The Cassini cosmic dust analyzer *Space Sci. Rev.* **114** 465

[2] Grün E, Fechtig H, Giese R H, Kissel J, Linkert D, Maas D, McDonnell J A M, Morfill G E, Schwehm G and Zook H A 1992 The Ulysses dust experiment *Astron. Astrophys. Suppl. Ser.* **92** 411

[3] Kissel J, Krueger F R, Silén J and Clark B C 2004 The cometary and interstellar dust analyzer at comet 81P/Wild 2 *Science* **304** 1774

[4] Kissel J *et al* 1986 Composition of comet Halley dust particles from Vega observations *Nature* **321** 336

[5] Dalmann B K, Grün E, Kissel J and Dietzel H 1977 The ion-composition of the plasma produced by impacts of fast dust particles *Planet. Space Sci.* **25** 135

[6] Burchell M J *et al* 2008 Characteristics of cometary dust tracks in Stardust aerogel and laboratory calibrations *Meteorit. Planet. Sci.* **43** 23

[7] Shu A *et al* 2012 3 MV hypervelocity dust accelerator at the Colorado center for lunar dust and atmospheric studies *Rev. Sci. Instrum.* **83** 075108

[8] Stübig M, Schäfer G, Ho T-M, Srama R and Grün E 2001 Laboratory simulation improvements for hypervelocity micrometeorite impacts with a new dust particle source *Planet. Space Sci.* **49** 853

[9] Mocker A *et al* 2011 A 2 mV van de Graaff accelerator as a tool for planetary and impact physics research *Rev. Sci. Instrum.* **82** 095111

[10] Duncan N, Sternovsky Z, Grün E, Auer S, Horanyi M, Drake K, Xie J, Lawrence G, Hansen D and Le H 2011 The electrostatic lunar dust analyzer (ELDA) for the detection and trajectory measurement of slow-moving dust particles from the lunar surface *Planet. Space Sci.* **59** 1446

[11] Xie J, Sternovsky Z, Grün E, Auer S, Duncan N, Drake K, Le H, Mihalyi H and Srama R 2011 Dust trajectory sensor: accuracy and data analysis *Rev. Sci. Instrum.* **82** 105104

[12] Auer S 1975 Two high resolution velocity vector analyzers for cosmic dust particles *Rev. Sci. Instrum.* **622** 127

[13] Auer S, Grün E, Kempf S, Srama R, Srowig A, Sternovsky Z and Tschernjawsk V 2008 Characteristics of a dust trajectory sensor *Rev. Sci. Instrum.* **79** 084501

[14] Auer S, Lawrence G, Grün E, Henkel H, Kempf S, Srama R and Sternovsky Z 2010 A self-triggered dust trajectory sensor *Nucl. Instrum. Methods* A **46** 74